

Viability of Sub-TeV Higgsino Dark Matter with Slepton Coannihilation

Yuanfang Yue^a, Yuetao Wang^a

^a *School of Physics, Henan Normal University, Xinxiang 453007, China*

E-mail: yueyuanfang@htu.edu.cn, wangyuetao@stu.htu.edu.cn

ABSTRACT: The higgsino-like neutralino is a compelling dark matter candidate motivated by both cosmology and naturalness considerations. While a pure higgsino typically requires a mass of around 1.1 TeV to satisfy the observed thermal relic abundance, the presence of light sleptons can significantly alter this requirement. In this work, we revisit higgsino dark matter within the Minimal Supersymmetric Standard Model (MSSM), focusing on scenarios with slepton coannihilation. We find that efficient coannihilation allows the higgsino mass to be as light as ~ 400 GeV while satisfying relic density constraints. We explicitly contrast the impact of recent direct detection updates: the LZ-2022 limits raise this lower bound to approximately 450 GeV, while the stringent LZ-2024 constraints further shift the viable mass floor to ~ 500 GeV. Crucially, we demonstrate that the direct detection sensitivity is strongly dependent on the relative signs of the gaugino mass parameters M_1 and M_2 . We find that scenarios with $M_1, M_2 > 0$ are fully excluded by LZ-2024. Conversely, configurations with opposite signs ($M_1/M_2 < 0$) remain broadly viable, as destructive interference in the neutralino-Higgs coupling efficiently suppresses the spin-independent cross section. Finally, we delineate the remaining viable parameter space for both the opposite-sign cases and the specific configurations with negative M_1 and M_2 .

Contents

1	Introduction	1
2	Theoretical Preliminaries	3
2.1	The Higgs and Neutralino Sectors	3
2.2	Dark Matter Relic Density	5
2.3	Dark Matter Direct Detection	6
3	Numerical Study	7
3.1	Research Strategy	8
3.2	Numerical Results and Discussion	10
3.2.1	DM annihilation	10
3.2.2	Impact of M_1 and M_2 on Direct Detection	13
4	Benchmark Points	16
5	Conclusion	18

1 Introduction

For decades, compelling evidence for dark matter (DM) has accumulated from a wide range of astrophysical and cosmological observations [1–7], yet its fundamental nature remains one of the most profound puzzles in modern physics. Weakly Interacting Massive Particles (WIMPs) arising from new physics at the TeV scale provide an elegant explanation, and among the most well-motivated frameworks is Supersymmetry (SUSY). In the Minimal Supersymmetric Standard Model (MSSM) [8–13], the lightest neutralino, a mixture of the bino, wino, and higgsinos, serves as a natural DM candidate.

However, the pure states of neutralino DM face opposing phenomenological challenges. A bino-like neutralino typically possesses a small annihilation cross-section, leading to an over-abundance of relic density unless specific mechanisms, such as coannihilation with scalars or resonant annihilation, enhance the annihilation rate [14]. Conversely, wino-like and pure higgsino-like neutralinos annihilate efficiently via electroweak interactions. A wino-like DM is typically under-abundant unless its mass is around 2.5 TeV [15], and it is severely constrained by indirect and direct detection searches [16–18]. Similarly, a pure higgsino is typically under-abundant unless its mass is raised to approximately 1.1 TeV [19–21]. This heavy

thermal mass target renders the pure higgsino largely inaccessible to current collider experiments.

Despite these challenges, the higgsino remains a prime DM candidate in both particle physics and cosmology communities [19, 20, 22–33]. Theoretically, it is appealing due to its connection to electroweak naturalness via the μ parameter [34–39] and its role as a realization of minimal dark matter [40], which can easily be embedded in frameworks like Split-SUSY [41–44]. The key difficulty remains its large annihilation cross-section in the sub-TeV regime, which results in a relic density far below the observed value [19, 21, 41, 45–48].

In this work, we focus on a realistic MSSM scenario where the dark matter is higgsino-dominated but possesses non-negligible bino and wino admixtures. We investigate how the synergy between this three-component mixing and slepton coannihilation [14, 49, 50] enables the correct relic density to be achieved for DM masses significantly below the 1 TeV thermal target—specifically extending down to ~ 400 GeV. Reviving this sub-TeV window is crucial as it brings the higgsino candidate back within the reach of experimental searches. It is important to distinguish this setup from the standard well-tempered neutralino scenario [45]. While well-tempered models rely solely on fine-tuning the mixing angles to satisfy relic density, our approach utilizes slepton coannihilation as an essential mechanism. This opens up a broader and lighter parameter space that would otherwise be forbidden in a purely well-tempered framework.

Higgsino coannihilation with sleptons has been previously investigated, for instance in Ref. [51], which found a lower mass limit of around 600 GeV under LUX 2016 constraints with fixed $\tan\beta \approx 10$. In this work, we revisit this scenario by performing a comprehensive scan over the parameter space, allowing $\tan\beta$ to vary and applying the latest, far more restrictive limits from the LZ 2022 and LZ 2024 experiments [52, 53]. We find that the DM mass can still be as low as ~ 500 GeV, provided that the model resides in specific interference regions determined by the relative signs of M_1 and M_2 .

The presence of bino and wino components is particularly consequential for these direct detection limits. The spin-independent scattering rate is governed by the interference between the bino and wino contributions to the neutralino-Higgs coupling. As hinted above, the relative signs of the mass parameters M_1 and M_2 dictate whether this interference is constructive or destructive. This suppression mechanism is analogous to the well-known blind spot phenomenon discussed in well-tempered scenarios [54–56]. However, a key distinction in our work is that the relic density is satisfied via slepton coannihilation rather than pure gaugino-higgsino mixing. Consequently, we identify viable “blind spot-like” regions in parameter space that are distinct from those found in standard well-tempered models, allowing the dark matter to evade even the stringent constraints from the LZ-2024 experiment.

It is worth noting that in the extreme decoupling limit, where gaugino masses

are very heavy, the mass splittings between higgsino states can become extremely small, opening up the possibility of inelastic scattering signatures [57, 58], which are themselves tightly constrained [59]. However, in the mixed scenario we consider, our focus remains on the elastic scattering interference effects which are most relevant for current direct detection limits.

This work is organized as follows. In Section 2, we review the theoretical framework and establish our notation. In Section 3, we detail our numerical scan strategy and present the main results. We showcase several representative benchmark points in Section 4. Finally, we summarize our findings and conclude in Section 5.

2 Theoretical Preliminaries

Dark matter physics within the MSSM is inextricably linked to the Higgs, neutralino, and chargino sectors. In this section, we briefly review the relevant theoretical framework, outlining the mass spectra and mixing structures of these sectors, which are fundamental to the calculation of the dark matter relic density and direct detection cross sections.

2.1 The Higgs and Neutralino Sectors

The Higgs sector of the MSSM consists of two Higgs doublets H_u and H_d . After electroweak symmetry breaking (EWSB), the neutral components of these doublets acquire vacuum expectation values (VEVs), denoted as v_u and v_d respectively. Phenomenological studies conventionally define the ratio of these VEVs as $\tan \beta = v_u/v_d$. To obtain the mass eigenstates, the neutral scalar fields are expanded around their VEVs as $H_k^0 = v_k + \frac{1}{\sqrt{2}}(S_k + iP_k)$ for $k = d, u$. The CP-even Higgs mass eigenstates h and H are obtained by rotating the interaction eigenstates S_d and S_u by the mixing angle α

$$\begin{pmatrix} h \\ H \end{pmatrix} = \begin{pmatrix} -\sin \alpha & \cos \alpha \\ \cos \alpha & \sin \alpha \end{pmatrix} \begin{pmatrix} S_d \\ S_u \end{pmatrix} \quad (2.1)$$

Here, h is identified as the SM-like Higgs boson with a mass of approximately 125 GeV, while H represents the heavy CP-even Higgs boson. In this work, we assume a decoupling limit where the heavier Higgs bosons are sufficiently massive to be removed from the low-energy spectrum, thereby focusing our analysis on the properties and interactions of the SM-like Higgs boson.

The neutralino sector is composed of four Majorana fermions resulting from the mixing of the neutral bino, wino, and higgsino fields. In the gauge eigenstate basis $\psi_j^0 = (\tilde{B}, \tilde{W}^0, \tilde{H}_d^0, \tilde{H}_u^0)$, the neutralino mass matrix is given by [12]:

$$M_{\tilde{\chi}^0} = \begin{pmatrix} M_1 & 0 & -\cos\beta\sin\theta_W m_Z & \sin\beta\sin\theta_W m_Z \\ 0 & M_2 & \cos\beta\cos\theta_W m_Z & -\sin\beta\cos\theta_W m_Z \\ -\cos\beta\sin\theta_W m_Z & \cos\beta\cos\theta_W m_Z & 0 & -\mu \\ \sin\beta\sin\theta_W m_Z & -\sin\beta\cos\theta_W m_Z & -\mu & 0 \end{pmatrix} \quad (2.2)$$

Here, M_1 and M_2 are the soft SUSY-breaking gaugino mass parameters associated with the $U(1)_Y$ and $SU(2)_L$ gauge groups respectively; μ is the higgsino mass parameter; θ_W is the weak mixing angle; and m_Z is the Z boson mass.

The neutralino mass matrix $M_{\tilde{\chi}^0}$ is diagonalized by a unitary matrix N to yield the physical masses $m_{\tilde{\chi}_i^0}$

$$N^* M_{\tilde{\chi}^0} N^{-1} = \text{diag}(m_{\tilde{\chi}_1^0}, m_{\tilde{\chi}_2^0}, m_{\tilde{\chi}_3^0}, m_{\tilde{\chi}_4^0}). \quad (2.3)$$

The mass eigenstates $\tilde{\chi}_i^0$ (ordered by mass such that $m_{\tilde{\chi}_1^0} < \dots < m_{\tilde{\chi}_4^0}$) are related to the gauge eigenstates via

$$\tilde{\chi}_i^0 = N_{ij} \psi_j^0. \quad (2.4)$$

In the MSSM, the lightest neutralino $\tilde{\chi}_1^0$ acts as a compelling dark matter candidate. Its composition is expressed as

$$\tilde{\chi}_1^0 = N_{11} \tilde{B} + N_{12} \tilde{W}^0 + N_{13} \tilde{H}_d^0 + N_{14} \tilde{H}_u^0. \quad (2.5)$$

The physical nature of the lightest neutralino is determined by its dominant component. It is classified as bino-like, wino-like, or higgsino-like if the largest contribution comes from $|N_{11}|^2$, $|N_{12}|^2$, or $|N_{13}|^2 + |N_{14}|^2$ respectively. This work specifically investigates the higgsino-like scenario.

The chargino sector consists of two Dirac fermions, formed by the mixing of the charged wino and higgsino components. In the basis $\psi^+ = (\tilde{W}^+, \tilde{H}_u^+)$ and $\psi^- = (\tilde{W}^-, \tilde{H}_d^-)$, the chargino mass matrix reads [12]

$$M_{\tilde{\chi}^\pm} = \begin{pmatrix} M_2 & \sqrt{2} \sin\beta m_W \\ \sqrt{2} \cos\beta m_W & \mu \end{pmatrix}, \quad (2.6)$$

where m_W is the W boson mass. The chargino mass eigenstates $\tilde{\chi}_i^\pm$ ($i = 1, 2$) are related to the gauge eigenstates through two unitary matrices U and V

$$\tilde{\chi}_i^+ = V_{ij} \psi_j^+, \quad \tilde{\chi}_i^- = U_{ij} \psi_j^-. \quad (2.7)$$

The diagonalization condition is given by:

$$U^* M_{\tilde{\chi}^\pm} V^{-1} = \text{diag}(m_{\tilde{\chi}_1^\pm}, m_{\tilde{\chi}_2^\pm}). \quad (2.8)$$

In the limit $|\mu| \ll M_1, M_2$, the lightest neutralino becomes predominantly higgsino-like. Consequently, the masses of $\tilde{\chi}_1^0$, $\tilde{\chi}_2^0$, and $\tilde{\chi}_1^\pm$ become nearly degenerate, all approximating the value $|\mu|$. This mass degeneracy is critical for the relic density calculation, as it enhances co-annihilation channels.

However, even in the higgsino-dominated regime, the bino and wino soft-breaking mass parameters M_1 and M_2 play a significant role in dark matter phenomenology. They induce mixing that affects the couplings to the Higgs and Z bosons, thereby significantly impacting the relic density and direct detection cross sections. The interplay between these gaugino masses and the higgsino parameter μ —especially under the stringent constraints from LZ2024—will be a key focus of our analysis.

2.2 Dark Matter Relic Density

The relic abundance of dark matter serves as a pivotal observable for constraining the parameter space of BSM physics. In the standard thermal freeze-out paradigm, the relic density is governed by the annihilation interactions of dark matter particles in the early universe. The time evolution of the dark matter number density n is described by the Boltzmann equation [22, 49, 60]

$$\frac{dn}{dt} + 3Hn = -\langle\sigma v\rangle(n^2 - n_{\text{eq}}^2), \quad (2.9)$$

where H is the Hubble parameter, $\langle\sigma v\rangle$ is the thermally averaged annihilation cross section multiplied by the relative velocity, and n_{eq} is the equilibrium number density. In the absence of co-annihilation effects, the relic density can be approximated as

$$\Omega h^2 \simeq 0.12 \left(\frac{80}{g_*}\right)^{1/2} \left(\frac{x_F}{25}\right) \left(\frac{2.3 \times 10^{-26} \text{ cm}^3/\text{s}}{\langle\sigma v\rangle_{x_F}}\right), \quad (2.10)$$

where g_* is the effective number of relativistic degrees of freedom at freeze-out, and $x_F \equiv m_{\text{DM}}/T_F$, with T_F being the freeze-out temperature [61].

However, when the dark matter candidate is part of a compressed mass spectrum, co-annihilation effects become significant and must be incorporated. This occurs when other sparticles χ_i have masses nearly degenerate with the lightest supersymmetric particle (LSP) χ_1 (where $m_{\chi_1} < m_{\chi_2} < \dots$).¹ Under these conditions, the standard thermally averaged cross section in the Boltzmann equation is replaced by an effective annihilation cross section $\langle\sigma v\rangle_{\text{eff}}$ defined as [49]

$$\langle\sigma v\rangle_{\text{eff}} = \sum_{i,j} \langle\sigma_{ij} v\rangle \frac{g_i g_j}{g_{\text{eff}}^2} (1 + \Delta_i)^{3/2} (1 + \Delta_j)^{3/2} \times \exp[-x(\Delta_i + \Delta_j)], \quad (2.11)$$

¹In our specific context, χ_1 corresponds to the LSP $\tilde{\chi}_1^0$, while χ_i ($i > 1$) represents the NLSPs, such as $\tilde{\chi}_1^\pm$ and $\tilde{\chi}_2^0$, which exhibit a small mass splitting with the LSP.

where the summation runs over all relevant co-annihilating species. Here $\langle \sigma_{ij} v \rangle$ denotes the thermally averaged cross section for the process $\chi_i \chi_j \rightarrow XX'$ (with X, X' being SM particles). The mass splitting parameter is defined as $\Delta_i = (m_{\chi_i} - m_{\chi_1})/m_{\chi_1}$, and g_i represents the internal degrees of freedom of particle χ_i . The effective degrees of freedom g_{eff} is given by [49]

$$g_{\text{eff}} = \sum_i g_i (1 + \Delta_i)^{3/2} \exp(-x\Delta_i). \quad (2.12)$$

Equation (2.12) implies that contributions from co-annihilating partners are exponentially suppressed by their mass splitting Δ_i . Therefore, only states that are nearly degenerate with the LSP play a significant role in determining the effective cross section and the resulting relic density.

A distinctive feature of our analysis is the inclusion of light sleptons in the spectrum. In standard scenarios where co-annihilation is restricted solely to the $\tilde{\chi}_2^0$ and $\tilde{\chi}_1^\pm$, it is rather difficult to realize a relatively light Higgsino dark matter candidate consistent with the observed relic density. However, in this work, we explicitly explore the parameter space where sleptons are sufficiently light to participate in the freeze-out process. The introduction of these additional slepton co-annihilation channels significantly modifies the effective annihilation cross section. A key objective of this study is to investigate how these channels impact the lower bound of the dark matter mass, specifically determining whether the presence of light sleptons renders lighter Higgsino dark matter phenomenologically viable under the stringent constraints of LZ2024.

2.3 Dark Matter Direct Detection

Direct detection experiments aim to observe dark matter particles through their elastic scattering off atomic nuclei in terrestrial detectors. This scattering process generally comprises two distinct components: spin-independent (SI) and spin-dependent (SD) interactions.

The dominant contribution to the SI scattering cross section typically arises from the t -channel exchange of CP-even Higgs bosons, assuming that squarks are sufficiently heavy. The SI cross section for dark matter scattering off a nucleon N can be expressed as [60]

$$\sigma^{\text{SI}} = \frac{4}{\pi} \left(\frac{m_{\tilde{\chi}_1^0} m_N}{m_{\tilde{\chi}_1^0} + m_N} \right)^2 f_N^2, \quad (2.13)$$

where $m_{\tilde{\chi}_1^0}$ is the dark matter mass, m_N is the nucleon mass, and f_N represents the effective scalar coupling between the dark matter particle and the nucleon. This effective coupling is given by

$$f_N = \sum_i \frac{C_{\tilde{\chi}_1^0 \tilde{\chi}_1^0 h_i} C_{h_i NN}}{m_{h_i}^2}, \quad (2.14)$$

where the summation runs over all CP-even Higgs eigenstates. In our framework, assuming the heavier Higgs bosons are decoupled, only the SM-like Higgs boson h contributes significantly. In the higgsino-dominated limit, the tree-level coupling of the lightest neutralino to the SM-like Higgs is approximated as [62]

$$C_{\tilde{\chi}_1^0 \tilde{\chi}_1^0 h} \approx \mp \frac{1}{2} m_W \left[\frac{\tan^2 \theta_W}{M_1 - |\mu|} + \frac{1}{M_2 - |\mu|} \right] (1 \pm \sin 2\beta), \quad (2.15)$$

with the upper(lower) sign corresponding to $\mu > 0 (\mu < 0)$. Given that $|M_{1,2}| \gg |\mu|$, the relative signs of M_1 and M_2 are crucial. Same-sign parameters lead to constructive interference in the bracket, enhancing the coupling, whereas opposite signs cause destructive interference. Additionally, the coupling naturally decouples as the gaugino masses M_1 and M_2 increase.

The SD scattering process is primarily mediated by the t -channel exchange of the Z boson in the heavy squark limit. The relevant axial-vector coupling in the pure higgsino limit is given by [62]

$$C_{\tilde{\chi}_1^0 \tilde{\chi}_1^0 Z} \simeq \mp \frac{1}{2\mu} m_W^2 \left(\frac{\tan^2 \theta_W}{M_1} + \frac{1}{M_2} \right) \cos 2\beta \quad (2.16)$$

This coupling exhibits a parametric dependence analogous to the SI case: it is suppressed by heavy gauginos and maximizes (minimizes) when M_1 and M_2 have the same (opposite) signs.

In summary, the direct detection sensitivity is critically dependent on the interplay between M_1 and M_2 . Scenarios with opposite-sign gaugino masses benefit from suppressed effective couplings, offering a mechanism to evade detection. Conversely, the constructive interference in same-sign scenarios makes them highly susceptible to experimental bounds. Consequently, the stringent constraints from LZ2024 are expected to exclude a significant portion of the same-sign parameter space, a feature we will examine closely in the following numerical analysis.

3 Numerical Study

In this section, we present our numerical study of Higgsino-like dark matter within the framework of the MSSM. We begin by outlining our research strategy, detailing the parameter space scan and the applied constraints. Subsequently, we present and discuss our numerical results, emphasizing the impact of coannihilation effects on the lower bound of DM mass and the roles of M_1 and M_2 in determining the direct detection cross-sections.

3.1 Research Strategy

We explore the parameter space using the `EasyScan_HEP` package [63], which implements the parallelized `MultiNest` algorithm [64] for efficient sampling. The relevant model parameters are varied within the ranges specified in Table 1. The rationale behind these parameter choices is detailed below

- **Higgsino Mass Parameter (μ)** The Higgsino mass parameter μ is scanned from 400 GeV to 1200 GeV. This interval covers the spectrum from the canonical thermal relic mass of ~ 1.1 TeV down to the sub-TeV regime, allowing us to investigate the viability of lighter Higgsino dark matter. To efficiently probe the phenomenologically interesting lower mass region while satisfying the stringent relic density and direct detection constraints, we adopt a segmented scanning strategy. The sub-TeV range is divided into multiple intervals: $\mu \in (400, 500), (500, 600), \dots, (900, 1000)$ GeV, followed by a final segment of $(1000, 1200)$ GeV. This approach ensures sufficient sampling density in the low-mass region where co-annihilation effects are most critical.
- **$\tan \beta$ and Trilinear Parameters (A_t, A_b)** The ratio of vacuum expectation values $\tan \beta$ is varied between 3 and 30. The lower bound is chosen to facilitate the realization of the 125 GeV Higgs mass and to satisfy LEP constraints on the Higgs sector [65]. The upper bound is restricted to avoid color-breaking minima and to ensure vacuum stability [66, 67]. The trilinear soft-breaking parameter A_t is scanned in the range of 2500 GeV to 5000 GeV to provide sufficient radiative corrections for the SM-like Higgs mass. For simplicity, we assume the relation $A_b = A_t$.
- **CP-odd Higgs Mass (m_A)** The mass of the CP-odd Higgs boson m_A is constrained to be greater than 500 GeV to evade exclusion limits from heavy Higgs searches [68]. An upper bound of 2000 GeV is imposed to maintain consistency with flavor physics constraints [67, 69].
- **Gaugino Mass Parameters (M_1, M_2)** The soft-breaking gaugino masses M_1 and M_2 are varied freely within the range of $[-6000, 6000]$ GeV. This wide range allows for a comprehensive exploration of their impact on the dark matter relic density and direct detection cross sections, particularly through their influence on the neutralino mixing and couplings.
- **Slepton Mass Splitting (Δ_L)** To specifically investigate slepton co-annihilation effects, we parametrize the slepton spectrum relative to the LSP mass. We define a dimensionless mass splitting parameter Δ_L , such that the soft-breaking masses for the left-handed sleptons, right-handed sleptons, and sneutrinos are given by $m_{\tilde{l}_L} = m_{\tilde{l}_R} = m_{\tilde{\nu}_L} = m_{\tilde{\chi}_1^0}(1 + \Delta_L)$. Δ_L is varied from 0 to 0.35, as co-annihilation becomes negligible for larger mass splittings. Other soft-breaking

masses, including squark masses and the gluino mass parameter M_3 , are decoupled by fixing them at 3 TeV to isolate the physics of the electroweakino-slepton sector.

The parameter ranges defined above represent a targeted estimation based on physical considerations, designed to maximize the likelihood of finding viable points that satisfy all experimental constraints. With these ranges established, we construct the global likelihood function as follows

$$\mathcal{L} \equiv \mathcal{L}_{\Omega h^2} \times \mathcal{L}_{\text{LZ2022}} \times \mathcal{L}_{\text{const.}} \quad (3.1)$$

This total likelihood function is a product of individual likelihoods corresponding to the dark matter relic density, direct detection limits, and other physical constraints.

For the relic density likelihood, $\mathcal{L}_{\Omega h^2}$, we adopt a Gaussian distribution centered at the Planck observed value $\Omega h^2 = 0.12$, with a conservative theoretical uncertainty of 10% [70]. The direct detection likelihood $\mathcal{L}_{\text{LZ2022}}$ is modeled as a one-sided Gaussian with a mean of zero and a variance defined by $\delta_\sigma = \sigma_{\text{UL}}^2/1.64^2 + (0.2\sigma)^2$ (incorporating a 20% theoretical uncertainty), where σ_{UL} denotes the 90% confidence level upper limit from the LZ 2022 experiment [52].

The term $\mathcal{L}_{\text{const}}$ enforces hard constraints by assigning a negligible likelihood to parameter points that violate any of the following conditions

- **Higgs Sector Constraints** The SM-like Higgs boson mass is required to fall within the window of 125 ± 3 GeV (i.e., 122–128 GeV), accounting for both experimental measurements and theoretical uncertainties in the spectrum calculation. Furthermore, constraints from Higgs searches and signal strength measurements are applied using HiggsBounds-5.11.3 [71–73], HiggsSignals-2.6.1[74–78], and HiggsTools-2.2.0 [79]. We require all accepted points to pass the exclusion checks provided by these tools.
- **Flavor Physics Constraints** Flavor observables, including $\text{BR}(B \rightarrow X_s \gamma)$ and $\text{BR}(B_s \rightarrow \mu^+ \mu^-)$, are calculated using FlavorKit [80]. We require these predictions to be consistent with experimental values [81] within a 2σ confidence interval.
- **Higgsino Composition** To ensure the analysis focuses on the higgsino-dominated scenario, we impose a filter requiring the higgsino fraction of the LSP, defined as $|N_{13}|^2 + |N_{14}|^2$, to be greater than 0.5.

To facilitate these calculations, we generated model files for SPheno-4.0.5[82–84] and MicrOMEGAs-5.0.4 [85–90] using SARAH-4.15.4[91–94]. For each input point, SPheno computes the mass spectrum and mixing matrices, while MicrOMEGAs is

Parameter	Prior	Range	Parameter	Prior	Range
μ/GeV	Flat	400–1200	$\tan\beta$	Flat	3–30
m_A/GeV	Flat	500–2000	M_1/GeV	Flat	–6000–6000
A_t/GeV	Flat	2500–5000	M_2/GeV	Flat	–6000–6000
Δ_L/GeV	Flat	0–0.35	–	–	–

Table 1. Parameter space explored in this study. We fixed trilinear coefficient $A_b = A_t$ for simplicity. The squark soft breaking mass are all fixed at 2000 GeV. M_1 and M_2 are soft breaking mass parameters for bino and wino. The gluino mass parameters M_3 are fixed at 3000 GeV. Δ_L is defined as the mass splitting between DM and sleptons. For other information, please refer to the text.

utilized to evaluate the dark matter relic density and both SI and SD scattering cross sections.

3.2 Numerical Results and Discussion

3.2.1 DM anihilation

Following a comprehensive scan of the parameter space, we generated a dataset containing approximately 1.1×10^6 points. In this section, we systematically evaluate these points by progressively imposing phenomenological and experimental constraints to quantify the impact of direct detection limits. Given that the LZ 2024 SI limits are significantly more stringent than the 2022 release, we explicitly compare the exclusion power of both datasets.

Figure 1 illustrates the predicted relic density as a function of the dark matter mass across four successive stages of constraints, as summarized in the caption. The Baseline constraints are constraints which are illustrated in \mathcal{L} constraints earlier, i.e. Higgs sector constraints, Flavor Physics Constraints as well as Higgsino constraints.

The progression of the panels clearly demonstrates the evolution of the lower bound on the dark matter mass. In the absence of direct detection limits (Top-Left), the relic density requirement alone (indicated by the horizontal blue band) permits dark matter masses as low as $m_\chi \gtrsim 400$ GeV. This deviation from the canonical ~ 1.1 TeV thermal higgsino limit is made possible by efficient co-annihilations with light sleptons.

Imposing the LZ 2022 SI constraint (Top-Right) excludes a portion of the low-mass parameter space, raising the effective lower bound to slightly above $m_\chi \sim 450$ GeV. Crucially, the more stringent LZ 2024 SI limit (Bottom-Left) further reduces the viable parameter space, shifting the lower mass bound to approximately 500 GeV. Note that in Figure 1, we focus solely on SI limits when discussing the DM mass floor, as SD constraints are substantially weaker in the higgsino-dominated regime and do not qualitatively alter the lower bound.

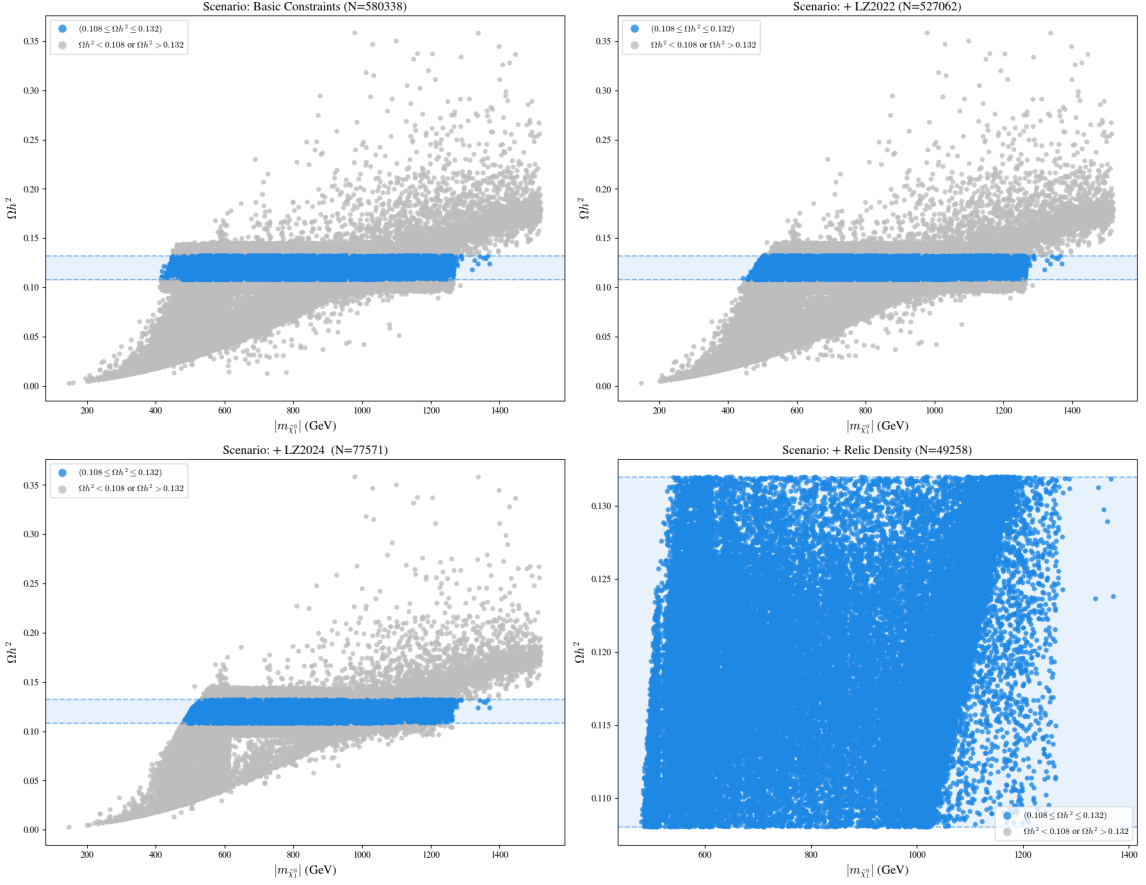


Figure 1. The predicted relic density as a function of DM mass for four successive stages of constraints: (Top-left) after applying our baseline cuts; (Top-right) adding the LZ2022 SI constraint; (Bottom-left) further imposing the stronger LZ2024 SI constraint; (Bottom-right) additionally imposing the relic-density requirement. Note that the bottom right panel is actually a zoomed-in version of the blue band for bottom-left panel.

For completeness, the number of surviving points after each stage is annotated in the header of each subplot. Starting from the raw sample, the Baseline cuts retain 580,338 points. The application of the LZ 2022 SI limit reduces this set to 527,062 points. However, the impact of the LZ 2024 SI limit is much more severe, leaving only 77,571 points. Finally, enforcing the strict relic density requirement (Bottom-Right) leaves a final sample of 49,258 points. This represents an $\simeq 90\%$ reduction relative to the post-baseline sample, highlighting the significant tension imposed by the latest direct detection results.

To elucidate the physical mechanisms governing the surviving parameter space further, particularly the role of slepton co-annihilation, we examine the mass splittings between the LSP and the next-to-lightest supersymmetric particles (NLSPs), specifically $\tilde{\chi}_2^0$, $\tilde{\chi}_1^\pm$, and the lightest slepton \tilde{l}_1 . The results are presented in Figure 2.

For this analysis, we employ the final dataset that satisfies *all* imposed con-

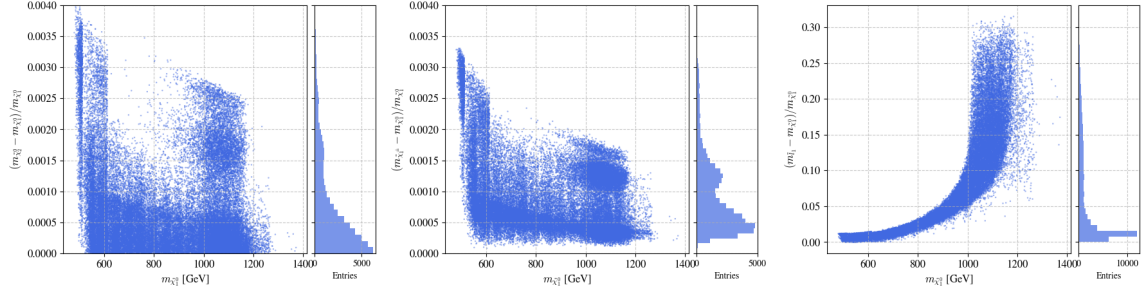


Figure 2. The mass splittings between $\tilde{\chi}_2^0$ and $\tilde{\chi}_1^0$ (left), between $\tilde{\chi}_1^\pm$ and $\tilde{\chi}_1^0$ (middle), and between the lightest slepton \tilde{l}_1 and $\tilde{\chi}_1^0$ (right) as functions of the LSP mass for the final sample that satisfies all constraints, including LZ2024 SI and SD limits as well as the relic density requirement. For each case, the left subplot shows the mass splitting versus the LSP mass, while the right shows the corresponding histogram of relative mass splittings.

straints, including the stringent LZ 2024 SI and SD limits as well as the relic density requirement. While SD constraints were omitted from the progressive evolution shown in Figure 1 for narrative clarity (as they do not determine the absolute lower mass bound), their inclusion here ensures a rigorous characterization of the final viable parameter space.

Figure 2 displays the relative mass splitting, defined as $\delta m = (m_{\text{NLSP}} - m_{\text{LSP}})/m_{\text{LSP}}$, between the LSP $\tilde{\chi}_1^0$ and its co-annihilation partners. The figure is divided into three panels corresponding to $\tilde{\chi}_2^0$ (left), $\tilde{\chi}_1^\pm$ (middle), and the lightest slepton \tilde{l}_1 (right). Each panel features a scatter plot of the mass splitting versus the LSP mass, accompanied by a marginal histogram illustrating the distribution of the splitting values.

Two distinct phenomenological regimes are immediately apparent from these distributions. The higgsino sector, depicted in the left and middle panels, is characterized by the expected high degree of degeneracy; the mass splittings for $\tilde{\chi}_2^0$ and $\tilde{\chi}_1^\pm$ typically remain below 1% across the entire dark matter mass range. In contrast, the slepton sector (right panel) exhibits a strong correlation between mass splitting and the dark matter mass. As the LSP mass decreases, the slepton mass splitting systematically drops, approaching near-exact degeneracy ($\delta m \rightarrow 0$) around 500 GeV. The sharp peaks in the histograms at low splitting values further confirm that a significant fraction of the valid points necessitate nearly degenerate sleptons.

This behaviour is directly linked to the mechanisms that set the dark matter relic abundance. For $m_{\tilde{\chi}_1^0} \sim 1$ TeV, the correct relic density is predominantly obtained through efficient co-annihilations within the nearly degenerate higgsino multiplet itself. In this regime, $\tilde{\chi}_2^0$ and $\tilde{\chi}_1^\pm$ remain close in mass to the LSP, and their annihilations into electroweak gauge bosons yield a large effective cross section $\langle\sigma v\rangle_{\text{eff}}$, while sleptons are sufficiently heavier that their contribution to freeze-out is negligible.

As the dark matter mass is lowered into the sub-TeV range, the higgsino DM would typically predict an even larger $\langle\sigma v\rangle_{\text{eff}}$ and thus an under-abundance of dark

matter. In our setup, this tendency is moderated by the presence of light sleptons that become increasingly degenerate with the LSP. In the parameter region selected by our scan, the slepton–slepton and slepton–higgsino (co-)annihilation cross sections are generally smaller than the dominant higgsino–higgsino channels. Consequently, when sleptons enter chemical equilibrium with the LSP and become nearly mass-degenerate, they increase the effective number of degrees of freedom during freeze-out without proportionally enhancing the total annihilation rate. This additional population of more weakly annihilating states acts to dilute the higgsino annihilation efficiency, effectively reducing $\langle \sigma v \rangle_{\text{eff}}$ relative to the pure-higgsino expectation and thereby raising the relic abundance to the observed cosmological value. The requirement that this dilution be sufficiently strong explains why the slepton mass splitting must shrink as $m_{\tilde{\chi}_1^0}$ approaches the ~ 500 GeV lower bound, as clearly seen in the right panel of Figure 2.

3.2.2 Impact of M_1 and M_2 on Direct Detection

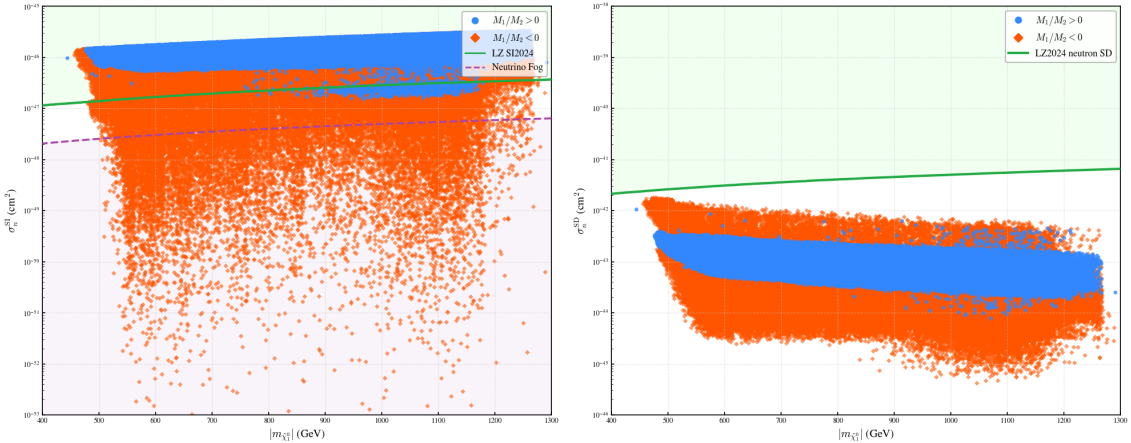


Figure 3. The SI(left pannel) and neutron SD(right pannel) cross section as a function of DM mass for samples that pass all constraints except LZ2024 SI limit. The shaded area above the green line is excluded by LZ2024 SI limit. Besides,we also plot the neutrino fog region below the dashed bright purple line for the left pannel. The orange and blue points represent the cases where M_1 and M_2 have the same sign and opposite sign respectively.

As previously discussed, the relative sign between the gaugino mass parameters M_1 and M_2 plays a decisive role in determining the direct detection scattering rates. To illustrate this dependence, Figure 3 presents both the SI and SD nucleon cross-sections for the parameter points that satisfy all prior constraints, including the LZ 2022 limits. The solid green lines denote the latest exclusion limits from the LZ 2024 experiment, allowing for a critical evaluation of their impact on scenarios with same-sign ($M_1/M_2 > 0$, blue circles) and opposite-sign ($M_1/M_2 < 0$, orange diamonds) gaugino masses.

In the left panel, the dichotomy in exclusion power between the two scenarios is striking. For the same-sign case(blue circles), the constructive interference in the LSP-Higgs coupling (Eq. 2.15) leads to generally enhanced scattering rates, which are now severely constrained by LZ 2024. This is particularly evident for dark matter masses below 800 GeV, where M_1 and M_2 are relatively light, resulting in significant gaugino-higgsino mixing and large cross-sections that are robustly excluded. However, a distinct cluster of points survives around 1 TeV. In this regime, the heavy mass scale of the gauginos ($M_{1,2} \gg \mu$) suppresses their admixture in the LSP state. Since the gaugino components enter the effective coupling inversely proportional to their masses, the scattering cross-section is naturally driven down. Consequently, these points approach the pure higgsino limit, where the suppressed coupling allows them to evade even the stringent LZ 2024 constraints despite the lack of destructive interference.

In sharp contrast, the opposite-sign case(orange diamonds) remains largely unconstrained by the new limits. This resilience is a direct consequence of destructive interference within the coupling structure, where the scattering amplitude can be suppressed by orders of magnitude regardless of the specific mass scale. A significant number of these points populate the region well below the current limit, with some extending down to the neutrino fog(indicated by the dashed purple line)—an irreducible background that poses a fundamental challenge for future direct detection experiments[95].

The right panel illustrates the SD neutron cross-section for the same dataset. Evidently, the current LZ 2024 SD limit is orders of magnitude weaker than the predicted rates and thus provides no effective constraints on this parameter space at present. Interestingly, however, the theoretical pattern mirrors that of the SI case: the same-sign scenario(blue circles) generally yields larger SD cross-sections than the opposite-sign counterpart(orange diamonds). This correlation exists because the Z -boson coupling (Eq. 2.16), which mediates the SD interaction, depends on the neutralino mixing matrices in a manner that exhibits analogous constructive or destructive tendencies governed by the relative signs of the gaugino masses.

To further illustrate the impact of the LZ2024 constraints, Figure 4 shows the distribution of our sampled parameter points in the (M_1, M_2) gaugino mass plane using hexagonal binning. Grey bins denote points that satisfy all constraints including the LZ2022 limits but are excluded once the LZ2024 results are imposed. Colored bins represent points that remain viable after applying the LZ2024 limits; the color scale encodes the mean value of the higgsino mass parameter μ in the left panel and of $\tan \beta$ in the right panel within each bin.

Comparing the grey and colored regions reveals a dramatic and highly asymmetric reshaping of the viable parameter space. Before imposing LZ2024, points with relatively light gauginos ($|M_1|, |M_2| \sim 2000$ GeV or even lower) were allowed across all four quadrants. However, the new constraints impose a severe penalty on regions

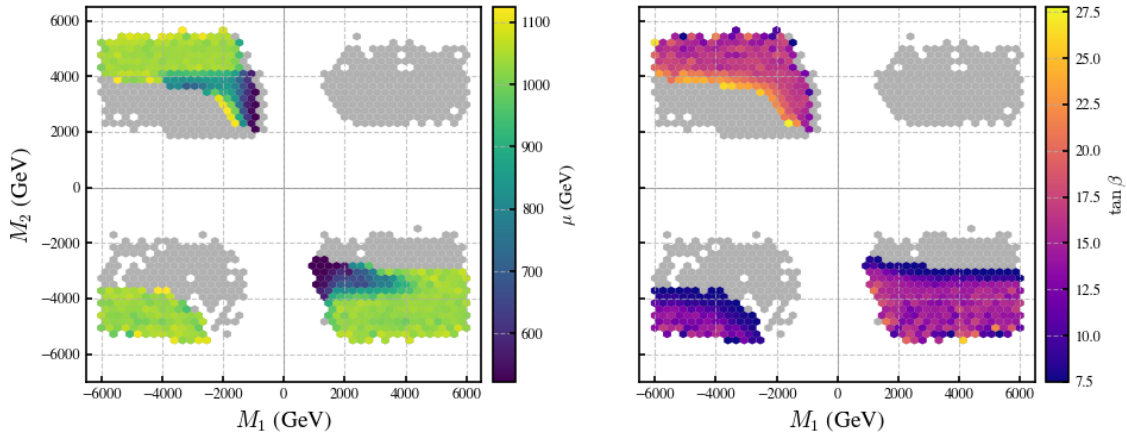


Figure 4. Distribution of the surviving parameter points in the M_1 - M_2 plane, visualized using hexagonal binning. The colored bins represent points that satisfy all constraints, including the latest LZ2024 results. The color scale indicates the mean value of μ (left panel) and $\tan\beta$ (right panel) within each bin. Grey bins denote points that were allowed by previous constraints (including LZ2022) but are now excluded by the LZ2024 results.

where M_1 and M_2 have the same sign. The first quadrant ($M_1, M_2 > 0$) is completely emptied, and in the third quadrant ($M_1, M_2 < 0$), the surviving points are pushed to very high masses ($|M_2| \gtrsim 4000$ GeV). In stark contrast, the opposite-sign quadrants ($M_1/M_2 < 0$) retain a much larger portion of the parameter space. While the lower bound on $|M_2|$ is lifted moderately (shifting towards 3000–4000 GeV as $|M_1|$ increases), light states with $|M_1| \sim 2000$ GeV and moderate $|M_2|$ remain viable.

This pronounced difference between the same-sign and opposite-sign regions points directly to the structure of the spin-independent DM–Higgs coupling. For a higgsino-like LSP this coupling contains two leading terms controlled by M_1 and M_2 , often associated with bino- and wino-like components. When M_1 and M_2 share the same sign, these M_1 - and M_2 -dependent terms add constructively, as seen in Eq. 2.15, leading to an enhanced SI cross-section that is now strongly ruled out by LZ2024.

Despite this overall trend, an asymmetry is visible between the two same-sign quadrants. The first quadrant is entirely removed by the new bound, whereas a small subset of points survives in the third quadrant. The surviving region is characterized by large gaugino masses, $|M_1|, |M_2| \gtrsim 2000$ GeV, higgsino mass parameters $|\mu|$ of order 1000 GeV that remain well below $|M_{1,2}|$, and comparatively small values of $\tan\beta$ within our scan range. The large $|M_{1,2}|$ suppresses the higgsino–gaugino mixing angles, leading to decoupling, while the smaller $\tan\beta$ values enhance $\sin 2\beta$, moving the coupling closer to the spin-independent blind-spot condition identified in Ref. [54], although it does not enforce an exact cancellation in our parameter range.

In contrast, the second and fourth quadrants ($M_1/M_2 < 0$) remain largely un-

constrained. Here the M_1 - and M_2 -dependent terms in the DM–Higgs coupling enter with opposite signs and partially cancel, which naturally suppresses the SI cross-section. This cancellation mechanism allows points with comparatively smaller gaugino masses $|M_1|, |M_2| \sim 2000\text{--}3000$ GeV, to remain viable after LZ2024. The left panel further shows that these surviving opposite-sign points with lower $|M_1|$ and $|M_2|$ tend to have smaller values of μ as well. This correlation is a direct consequence of our scan setup, which assumes $|\mu| \ll |M_1|, |M_2|$ in order to realize a higgsino-dominated LSP.

Overall, in the opposite-sign region $M_1/M_2 < 0$, the partial cancellation between the M_1 - and M_2 -dependent pieces of the DM–Higgs coupling leads to a pronounced suppression of the SI cross section. This pattern is qualitatively analogous to the direct-detection blind spots discussed in Ref. [54], although our surviving points do not lie on the exact blind-spot surfaces, which would require, for example, $M_{1,2} + \mu \sin 2\beta = 0$ or $\tan \beta = 1$. Instead, they are located in a decoupling regime with $|M_{1,2}| \gg |\mu|$ and moderate-to-large $\tan \beta$, where higgsino purity and partial cancellation between the M_1 and M_2 terms jointly drive the SI cross section below the LZ2024 limit.

4 Benchmark Points

To provide a concrete illustration of the phenomenology discussed above, we present four benchmark points in Table 2 and Table 3, corresponding to the first through fourth quadrants of Figure 4 respectively. Together they exemplify the different mechanisms that allow higgsino-like DM to satisfy the relic-density and direct-detection constraints in the same-sign and opposite-sign regions of (M_1, M_2) .

As shown in the tables, all four benchmarks feature a higgsino-dominated DM candidate, evidenced by the nearly mass-degenerate spectrum of $\tilde{\chi}_{1,2}^0$ and $\tilde{\chi}_1^\pm$ with masses close to the μ parameter. Point P1, characterized by positive M_1 and M_2 and a relatively light DM state, was permitted by LZ2022 but is now excluded by LZ2024. This behaviour directly reflects the discussion in Section 3.2: in the first quadrant the M_1 - and M_2 -dependent pieces of the DM–Higgs coupling add constructively, leading to a comparatively large SI cross section that has now been probed by the improved sensitivity of LZ2024.

In contrast, Point P3 lies in the same-sign region with large negative M_1 and M_2 and remains viable thanks to the decoupling of heavy gauginos. For P3, the DM mass is approximately 850.2 GeV. Although the mass splitting between the lightest slepton and the DM is about 30 GeV, the much smaller splittings (~ 2 GeV) with the other light higgsinos ensure that co-annihilation with $\tilde{\chi}_1^\pm$ and $\tilde{\chi}_2^0$ is the dominant mechanism for achieving the correct relic density. At the same time, the large $|M_{1,2}|$ values suppress the higgsino–gaugino mixing angles, and the relatively small $\tan \beta$ enhances $\sin 2\beta$, placing P3 in the decoupling regime identified in Figure 4

and moving it close to the spin-independent blind-spot condition of Ref. [54]. As a result, the effective DM–Higgs coupling, and hence the SI cross section, is strongly reduced.

Points P2 and P4 represent scenarios where M_1 and M_2 have opposite signs, corresponding to the cancellation regions in Figure 4. In both cases, the mass splittings between the DM and the other higgsinos are extremely small ($\lesssim 1$ GeV), making higgsino co-annihilation highly efficient. However, as the DM mass decreases from P2 (~ 602 GeV) to P4 (~ 498 GeV), the mass degeneracy with the lightest slepton becomes more pronounced. Consequently, the contribution from slepton co-annihilation channels increases from approximately 1.0% in P2 to about 2.3% in P4, while higgsino co-annihilation remains the dominant process in both cases. From the point of view of direct detection, the opposite signs of M_1 and M_2 imply that the M_1 - and M_2 -dependent terms in the DM–Higgs coupling partially cancel, in line with the behaviour seen in the second and fourth quadrants of Figure 4. This destructive interference suppresses the SI cross section even though the gaugino masses in P2 and P4 are smaller than in P3, illustrating the complementarity between decoupling and cancellation effects.

Overall, these benchmark points demonstrate a clear trend: as the higgsino-like DM mass decreases, co-annihilation with sleptons becomes increasingly important, although it still provides only a subdominant contribution compared to higgsino co-annihilation in our benchmarks. At the same time, they explicitly realize the three main mechanisms identified in Section 3.2: (i) constructive interference in the same-sign region leading to exclusion by LZ2024 (P1), (ii) suppression of the DM–Higgs coupling via gaugino decoupling and proximity to a blind spot (P3), and (iii) partial cancellation of the M_1 and M_2 contributions when $M_1/M_2 < 0$ (P2 and P4). This behaviour corroborates our numerical analysis in Section 3.2 and the trends shown in Figures 2 and 4.

In addition, we have checked all four benchmark points against the latest LHC 13 TeV electroweakino searches. The relevant production channels are $pp \rightarrow \tilde{\chi}_i^\pm \tilde{\chi}_j^\mp$, $pp \rightarrow \tilde{\chi}_i^0 \tilde{\chi}_j^0$, and $pp \rightarrow \tilde{\chi}_i^\pm \tilde{\chi}_j^0$ with $i, j = 1, 2$. We generate parton-level events with MadGraph5_aMC@NLO 2.9 [96, 97], perform parton shower and hadronization using Pythia 8.3 [98, 99], and simulate the detector response with Delphes-3.4 [100]. The resulting detector-level events are then passed to CheckMATE2 2.0.34 [101], which compares our signal predictions with the published ATLAS and CMS analyses and determines whether a given parameter point is excluded at 95% CL. For each benchmark we evaluate the CheckMATE variable $R = \max_i(S_i/S_i^{95})$, where S_i is the predicted signal yield in signal region i and S_i^{95} is the corresponding experimental upper limit. We find that the largest R value among our benchmarks is about 0.02, well below the exclusion threshold $R = 1$, so none of the points is currently ruled out by existing LHC searches. However, the High-Luminosity LHC(HL-LHC) and High Energy LHC(HE-LHC)[102], as well as future indirect searches[103, 104](e.g. with

Point P1		Point P2	
Parameter	Value	Parameter	Value
$\tan\beta$	18.68	$\tan\beta$	27.06
μ, m_A	483.90, 1254.38	μ, m_A	588.40, 1702.39
M_1, M_2	2470.27, 2665.33	M_1, M_2	-1195.71, 3337.25
A_t, Δ_L	4517.42, 0.14	A_t, Δ_L	2817.50, 0.18
Particle	Mass spectrum	Particle	Mass spectrum
$\tilde{\chi}_1^0, \tilde{\chi}_2^0$	494.6, -497.0	$\tilde{\chi}_1^0, \tilde{\chi}_2^0$	-601.7, 602.4
$\tilde{\chi}_3^0, \tilde{\chi}_4^0$	2465.2, 2642.8	$\tilde{\chi}_3^0, \tilde{\chi}_4^0$	-1191.8, 3296.9
$\tilde{\chi}_1^\pm, \tilde{\chi}_2^\pm$	496.0, 2642.9	$\tilde{\chi}_1^\pm, \tilde{\chi}_2^\pm$	601.7, 3296.9
\tilde{e}_L, h	494.7, 124.8	\tilde{e}_L, h	604.0, 125.0
H, A	1684.1, 1684.1	H, A	2178.6, 2178.6
Rotation matrix	Element value[%]	Rotation matrix	Element value[%]
$N_{11}, N_{12}, N_{13}, N_{14}$	-1.7, 2.6, -70.8, 70.6	$N_{11}, N_{12}, N_{13}, N_{14}$	5.1, 1.3, 70.7, 70.5
$N_{21}, N_{22}, N_{23}, N_{24}$	-1.0, 1.6, 70.6, 70.8	$N_{21}, N_{22}, N_{23}, N_{24}$	-1.8, -2.1, 70.7, -70.7
$N_{31}, N_{32}, N_{33}, N_{34}$	100.0, 1.0, -0.5, 1.8	$N_{31}, N_{32}, N_{33}, N_{34}$	99.9, -0.1, -2.3, -4.9
$N_{41}, N_{42}, N_{43}, N_{44}$	0.9, -100.0, -0.7, 3.1	$N_{41}, N_{42}, N_{43}, N_{44}$	0, -100, -0.5, 2.4
Primary annihilation	Fraction [%]	Primary annihilation	Fraction [%]
$\tilde{\chi}_1^0 \tilde{\chi}_1^- \rightarrow d\bar{u}/s\bar{c}/b\bar{t}/\bar{\nu}_e e/\bar{\nu}_\mu \mu/\bar{\nu}_\tau \tau$	22.4	$\tilde{\chi}_1^0 \tilde{\chi}_1^- \rightarrow d\bar{u}/s\bar{c}/b\bar{t}/\bar{\nu}_e e/\bar{\nu}_\mu \mu/\bar{\nu}_\tau \tau$	23.10
$\tilde{\chi}_2^0 \tilde{\chi}_1^- \rightarrow d\bar{u}/s\bar{c}/b\bar{t}/\bar{\nu}_e e/\bar{\nu}_\mu \mu/\bar{\nu}_\tau \tau$	14.8	$\tilde{\chi}_1^0 \tilde{\chi}_1^- \rightarrow \gamma W_1^-$	1.03
$\tilde{\chi}_1^0 \tilde{\chi}_1^0 \rightarrow W^- W^+/ZZ$	3.9	$\tilde{\chi}_2^0 \tilde{\chi}_1^- \rightarrow d\bar{u}/s\bar{c}/b\bar{t}/\bar{\nu}_e e/\bar{\nu}_\mu \mu/\bar{\nu}_\tau \tau$	18.93
$\tilde{\chi}_1^- \tilde{\chi}_1^+ \rightarrow u\bar{u}/c\bar{c}/t\bar{t}/d\bar{d}/s\bar{s}/W^- W^+$	8.9	$\tilde{\chi}_1^- \tilde{\chi}_1^+ \rightarrow u\bar{u}/c\bar{c}/t\bar{t}/d\bar{d}/s\bar{s}/W^- W^+$	9.40
$\tilde{\chi}_1^0 \tilde{\chi}_2^0 \rightarrow d\bar{d}/s\bar{s}/u\bar{u}/c\bar{c}/b\bar{b}$	7.5	$\tilde{\chi}_1^0 \tilde{\chi}_1^0 \rightarrow W^- W^+/ZZ$	5.30
$\tilde{e}_L \tilde{e}_L^* \rightarrow W^- W^+$	1.3	$\tilde{\chi}_1^0 \tilde{\chi}_2^0 \rightarrow u\bar{u}/c\bar{c}/d\bar{d}/s\bar{s}/b\bar{b}$	10.62
		$\tilde{\chi}_1^0 \tilde{\chi}_2^0 \rightarrow \nu\bar{\nu}_e/\nu_\mu \bar{\nu}_\mu/\nu_\tau \bar{\nu}_\tau$	3.19
		$\tilde{e}_L \tilde{\chi}_1^+ \rightarrow \tau W^-$	1.01
DM observable	Value	DM observable	Value
Ωh^2	0.118	Ωh^2	0.120
$\sigma_{p,n}^{\text{SI}}/(10^{-46} \text{cm}^2)$	1.40, 1.44	$\sigma_{p,n}^{\text{SI}}/(10^{-47} \text{cm}^2)$	1.24, 1.26
$\sigma_{p,n}^{\text{SD}}/(10^{-43} \text{cm}^2)$	3.39, 2.60	$\sigma_{p,n}^{\text{SD}}/(10^{-43} \text{cm}^2)$	1.44, 1.10

Table 2. Parameters for benchmark points P1 and P2, chosen from the first ($M_1, M_2 > 0$) and second ($M_1 < 0, M_2 > 0$) quadrants of Figure 4, respectively. Point P1 is representative of the grey region in its quadrant and is therefore excluded by the LZ2024 limits. In contrast, P2 is selected from the colored (allowed) region and remains a viable scenario. All parameters with mass dimensions are in GeV.

H.E.S.S. and future gamma-ray telescopes), will substantially improve the sensitivity to higgsino-like electroweakinos and could probe large parts of the parameter space illustrated by our benchmark points [105].

5 Conclusion

We performed a comprehensive analysis of higgsino-dominated dark matter within the MSSM framework, focusing on the implications of the latest LZ2024 direct-detection limits when slepton co-annihilation channels are taken into account. Including constraints from the Higgs sector, B -physics, and the DM relic density, we progressively applied the LZ2022 and LZ2024 SI and SD limits to illustrate their

Point P3		Point P4	
Parameter	Value	Parameter	Value
$\tan \beta$	8.28	$\tan \beta$	27.05
μ, m_A	833.09, 1147.13	μ, m_A	485.86, 1824.18
M_1, M_2	-4833.66, -4604.87	M_1, M_2	1330.40, -2926.88
A_t, Δ_L	3753.44, 0.28	A_t, Δ_L	2831.66, 0.17
Particle	Mass spectrum	Particle	Mass spectrum
$\tilde{\chi}_1^0, \tilde{\chi}_2^0$	-850.2, 852.6	$\tilde{\chi}_1^0, \tilde{\chi}_2^0$	-498.1, 498.9
$\tilde{\chi}_3^0, \tilde{\chi}_4^0$	-4551.2, -4868.2	$\tilde{\chi}_3^0, \tilde{\chi}_4^0$	1326.1, -2896.9
$\tilde{\chi}_1^\pm, \tilde{\chi}_2^\pm$	851.9, 4551.3	$\tilde{\chi}_1^\pm, \tilde{\chi}_2^\pm$	499.2, 2897.0
\tilde{e}_L, h	881.0, 125.4	\tilde{e}_L, h	498.3, 125.2
H, A	1151.1, 1165.1	H, A	1991.8, 1991.7
Rotation matrix	Element value [%]	Rotation matrix	Element value [%]
$N_{11}, N_{12}, N_{13}, N_{14}$	-0.7, 1.3, -70.8, -70.6	$N_{11}, N_{12}, N_{13}, N_{14}$	1.6, 2.2, -70.8, -70.6
$N_{21}, N_{22}, N_{23}, N_{24}$	0.6, -1.2, -70.7, 70.8	$N_{21}, N_{22}, N_{23}, N_{24}$	3.9, 1.7, 70.7, -70.6
$N_{31}, N_{32}, N_{33}, N_{34}$	0.2, 100.0, 0.1, 1.8	$N_{31}, N_{32}, N_{33}, N_{34}$	99.9, -0.1, -1.6, 3.9
$N_{41}, N_{42}, N_{43}, N_{44}$	-100.0, 0.2, 0.1, 0.9	$N_{41}, N_{42}, N_{43}, N_{44}$	0.100.0, -0.4, -2.8
Primary annihilation	Fraction [%]	Primary annihilation	Fraction [%]
$\tilde{\chi}_1^0 \tilde{\chi}_1^- \rightarrow d\bar{u}/s\bar{c}/b\bar{t}/\bar{\nu}_e e/\bar{\nu}_\mu \mu/\bar{\nu}_\tau \tau$	26.59	$\tilde{\chi}_1^0 \tilde{\chi}_1^- \rightarrow d\bar{u}/s\bar{c}/b\bar{t}/\bar{\nu}_e e/\bar{\nu}_\mu \mu/\bar{\nu}_\tau \tau$	20.49
$\tilde{\chi}_1^0 \tilde{\chi}_1^- \rightarrow \gamma W_1^-/ZW_1^-$	2.52	$\tilde{\chi}_2^0 \tilde{\chi}_1^- \rightarrow d\bar{u}/s\bar{c}/b\bar{t}/\bar{\nu}_e e/\bar{\nu}_\mu \mu/\bar{\nu}_\tau \tau$	17.63
$\tilde{\chi}_2^0 \tilde{\chi}_1^- \rightarrow d\bar{u}/s\bar{c}/b\bar{t}/\bar{\nu}_e e/\bar{\nu}_\mu \mu/\bar{\nu}_\tau \tau$	19.12	$\tilde{\chi}_1^- \tilde{\chi}_1^+ \rightarrow u\bar{u}/c\bar{c}/t\bar{t}/d\bar{d}/s\bar{s}/W^-W^+$	8.64
$\tilde{\chi}_1^- \tilde{\chi}_1^+ \rightarrow u\bar{u}/c\bar{c}/t\bar{t}/d\bar{d}/s\bar{s}$	10.36	$\tilde{\chi}_1^0 \tilde{\chi}_1^0 \rightarrow W^-W^+/ZZ$	3.01
$\tilde{\chi}_1^- \tilde{\chi}_1^+ \rightarrow W^-W^+/e\bar{e}/\mu\bar{\mu}/\tau\bar{\tau}$	5.98	$\tilde{\chi}_1^0 \tilde{\chi}_2^0 \rightarrow u\bar{u}/c\bar{c}/d\bar{d}/s\bar{s}/b\bar{b}$	8.73
$\tilde{\chi}_1^0 \tilde{\chi}_1^0 \rightarrow W^-W^+/ZZ$	5.09	$\tilde{e}_L \tilde{\chi}_1^- \rightarrow \tau W^-$	1.17
$\tilde{\chi}_1^0 \tilde{\chi}_2^0 \rightarrow d\bar{d}/s\bar{s}/b\bar{b}/u\bar{u}/c\bar{c}/t\bar{t}$	12.09	$\tilde{e}_L \tilde{e}_L^* \rightarrow W^-W^+$	1.14
$\tilde{\chi}_1^0 \tilde{\chi}_2^0 \rightarrow \bar{\nu}_e e/\bar{\nu}_\mu \mu/\bar{\nu}_\tau \tau$	3.08		
DM observable	Value	DM observable	Value
Ωh^2	0.118	Ωh^2	0.116
$\sigma_{p,n}^{\text{SI}}/(10^{-47} \text{cm}^2)$	1.82, 1.84	$\sigma_{p,n}^{\text{SI}}/(10^{-47} \text{cm}^2)$	1.37, 1.38
$\sigma_{p,n}^{\text{SD}}/(10^{-43} \text{cm}^2, 10^{-44} \text{cm}^2)$	1.05, 8.02	$\sigma_{p,n}^{\text{SD}}/(10^{-43} \text{cm}^2)$	1.46, 1.12

Table 3. Parameters for benchmark points P3 and P4. These points are selected from the colored(allowed) regions of the third ($M_1, M_2 < 0$) and fourth ($M_1 > 0, M_2 < 0$) quadrants of Figure 4 respectively. Consequently, both points are consistent with all current constraints, including the latest LZ2024 direct detection limits. The units of all mass parameters are given in GeV.

impact on the parameter space. Based on this analysis, we draw the following conclusions

- **Relic density and mass constraints** The relic-density requirement by itself typically favors a higgsino DM mass around 1 TeV, since the efficient annihilation of higgsino-like DM leads to an under-abundance at lower masses. Our study shows that, once slepton co-annihilation channels are included, the effective annihilation cross section is modified in such a way that the correct relic density can be achieved at significantly lower masses. Under the LZ2022 constraints, the allowed DM mass can be as low as ~ 400 GeV. After imposing the more stringent LZ2024 limits, this lower bound is raised to about 500 GeV. While slepton co-annihilation remains subdominant compared to $\tilde{\chi}_1^\pm$

and $\tilde{\chi}_2^0$ co-annihilation over most of the sub-TeV region, its relative importance grows as the DM mass decreases towards 500 GeV. In this mass window, even a subdominant slepton contribution can play a crucial role in satisfying the relic-density constraint.

- **Direct detection and interference effects** For DM–nucleon scattering, the absolute size of the SI and SD cross sections is suppressed by large gaugino masses (M_1 and M_2), but the relative sign between M_1 and M_2 has a pronounced impact through interference effects in the DM–Higgs and DM– Z couplings. When M_1 and M_2 have the same sign, constructive interference enhances the SI cross section, leading to strong constraints from LZ2024. Conversely, when M_1 and M_2 have opposite signs, destructive interference suppresses the SI cross section, allowing a much larger portion of the parameter space to evade current bounds. In particular, we find that the entire first quadrant ($M_1, M_2 > 0$) is excluded by LZ2024, whereas viable points survive in the third quadrant ($M_1, M_2 < 0$) thanks to gaugino decoupling and proximity to spin-independent blind spots. This sharp contrast between same-sign and opposite-sign regions constitutes one of the key qualitative outcomes of our analysis.

Regarding collider constraints, the mass splittings between the higgsino-like LSP and the other higgsino states ($\tilde{\chi}_2^0$ and $\tilde{\chi}_1^\pm$) in our scenarios are typically very small (below about 1%), leading to soft decay products that are challenging to detect. The sleptons involved in co-annihilation are also nearly degenerate with the LSP, resulting in similarly soft final states. As discussed in Section 4, a recast of the latest 13 TeV electroweakino searches with `CheckMATE2` yields $R \ll 1$ for all our benchmark points, so current LHC searches have limited sensitivity to such compressed spectra. Future collider experiments such as the HL-LHC or HE-LHC, as well as indirect searches will be promising to effectively probe the parameter space highlighted in this work.

Acknowledgement

This work is supported by the National Natural Science Foundation of China (NNSFC) under grant No. 12575110 and Natural Science Foundation of Henan Province under Grant No. 232300421217. We sincerely thank Prof. Junjie Cao and D.r. Zhiyang Bao for helpful discussions during this project.

References

- [1] F. Zwicky, *On the large scale distribution of matter in the universe*, *Physical Review* **61** (1942) 489.

[2] F. Zwicky, *Clusters of galaxies*, in *Astrophysik IV: Sternsysteme/Astrophysics IV: Stellar Systems*, pp. 390–415. Springer, 1959.

[3] F. Zwicky and M. Humason, *Spectra and other characteristics of interconnected galaxies and of galaxies in groups and in cluster. i.*, *Astrophysical Journal, vol. 132*, p. 627 **132** (1960) 627.

[4] V. Trimble, *Existence and nature of dark matter in the universe*, *Annual review of astronomy and astrophysics* **25** (1987) 425.

[5] R. H. Sanders, *The dark matter problem: A historical perspective*. Cambridge University Press, 2010.

[6] PLANCK collaboration, N. Aghanim et al., *Planck 2018 results. VI. Cosmological parameters*, *Astron. Astrophys.* **641** (2020) A6 [[1807.06209](#)].

[7] E. Pécontal, T. Buchert, P. Di Stefano, Y. Copin and K. Freese, *Review of observational evidence for dark matter in the universe and in upcoming searches for dark stars*, *European Astronomical Society Publications Series* **36** (2009) 113.

[8] H. P. Nilles, *Supersymmetry, Supergravity and Particle Physics*, *Phys. Rept.* **110** (1984) 1.

[9] H. E. Haber and G. L. Kane, *The Search for Supersymmetry: Probing Physics Beyond the Standard Model*, *Phys. Rept.* **117** (1985) 75.

[10] J. F. Gunion and H. E. Haber, *Higgs Bosons in Supersymmetric Models. 1.*, *Nucl. Phys. B* **272** (1986) 1.

[11] C. Csaki, *The minimal supersymmetric standard model*, *Modern Physics Letters A* **11** (1996) 599.

[12] S. P. Martin, *A Supersymmetry primer*, *Adv. Ser. Direct. High Energy Phys.* **18** (1998) 1 [[hep-ph/9709356](#)].

[13] H. E. Haber, *The status of the minimal supersymmetric standard model and beyond*, *Nuclear physics b-proceedings supplements* **62** (1998) 469.

[14] J. Edsjo and P. Gondolo, *Neutralino relic density including coannihilations*, *Phys. Rev. D* **56** (1997) 1879 [[hep-ph/9704361](#)].

[15] M. Beneke, A. Bharucha, A. Hryczuk, S. Recksiegel and P. Ruiz-Femenia, *The last refuge of mixed wino-Higgsino dark matter*, *Journal of High Energy Physics* **01** (2017) 002 [[1611.00804](#)].

[16] T. Cohen, M. Lisanti, A. Pierce and T. R. Slatyer, *Wino Dark Matter Under Siege*, *JCAP* **10** (2013) 061 [[1307.4082](#)].

[17] J. Fan and M. Reece, *In Wino Veritas? Indirect Searches Shed Light on Neutralino Dark Matter*, *JHEP* **10** (2013) 124 [[1307.4400](#)].

[18] B. R. Safdi and W. L. Xu, *Wino and Real Minimal Dark Matter Excluded by Fermi Gamma-Ray Observations*, [2507.15934](#).

- [19] A. Delgado and M. Quirós, *Higgsino Dark Matter in the MSSM*, *Phys. Rev. D* **103** (2021) 015024 [[2008.00954](#)].
- [20] K. Kowalska and E. M. Sessolo, *The discreet charm of higgsino dark matter - a pocket review*, *Adv. High Energy Phys.* **2018** (2018) 6828560 [[1802.04097](#)].
- [21] U. Chattopadhyay, D. Choudhury, M. Drees, P. Konar and D. P. Roy, *Looking for a Heavy Higgsino LSP in Collider and Dark Matter Experiments*, *Physics Letters B* **632** (2006) 114 [[hep-ph/0508098](#)].
- [22] G. Jungman, M. Kamionkowski and K. Griest, *Supersymmetric dark matter*, *Physics Reports* **333** (1995) 167.
- [23] G. L. Kane and J. D. Wells, *Higgsino Cold Dark Matter Motivated by Collider Data*, *Physical Review Letters* **76** (1996) 4458 [[hep-ph/9603336](#)].
- [24] M. Drees, M. M. Nojiri, D. P. Roy and Y. Yamada, *Light Higgsino Dark Matter*, *Physical Review D* **56** (1997) 276 [[hep-ph/9701219](#)].
- [25] M. Masip and I. Mastromatteo, *Higgsino dark matter in partly supersymmetric models*, *Physical Review D* **73** (2006) 015007 [[hep-ph/0510311](#)].
- [26] F. Wang, W. Wang and J. M. Yang, *Dark Matter Constraints on Gaugino/Higgsino Masses in Split Supersymmetry and Their Implications at Colliders*, *The European Physical Journal C* **46** (2006) 521 [[hep-ph/0512133](#)].
- [27] J. P. Hall and S. F. King, *Neutralino Dark Matter with Inert Higgsinos and Singlinos*, *Journal of High Energy Physics* **08** (2009) 088 [[0905.2696](#)].
- [28] K. Sinha, *Higgsino Dark Matter and the Cosmological Gravitino Problem*, *AIP Conf. Proc.* **1534** (2013) 146 [[1212.0011](#)].
- [29] V. E. Mayes and A. W. Lutz, *Light Higgsino Dark Matter in the MSSM on D-branes*, *Journal of Physics G: Nuclear and Particle Physics* **42** (2015) 095006 [[1412.1452](#)].
- [30] K. Wang and J. Zhu, *Investigating higgsino dark matter in the semi-constrained NMSSM**, *Chin. Phys. C* **48** (2024) 113101 [[2406.15939](#)].
- [31] J. L. Evans and K. A. Olive, *Higgsino Dark Matter in Pure Gravity Mediated Supersymmetry*, *Physical Review D* **106** (2022) 055026 [[2202.07830](#)].
- [32] N. Nagata and S. Shirai, *Higgsino dark matter in high-scale supersymmetry*, *Journal of High Energy Physics* **01** (2015) 029 [[1410.4549](#)].
- [33] L. Aparicio, M. Cicoli, B. Dutta, F. Muia and F. Quevedo, *Light Higgsino Dark Matter from Non-thermal Cosmology*, *JHEP* **11** (2016) 038 [[1607.00004](#)].
- [34] H. Baer, V. Barger, P. Huang and X. Tata, *Natural Supersymmetry: LHC, dark matter and ILC searches*, *JHEP* **05** (2012) 109 [[1203.5539](#)].
- [35] U. Ellwanger and C. Hugonie, *The higgsino–singlino sector of the NMSSM: combined constraints from dark matter and the LHC*, *Eur. Phys. J. C* **78** (2018) 735 [[1806.09478](#)].

[36] H. Baer, V. Barger, D. Sengupta and X. Tata, *Is natural higgsino-only dark matter excluded?*, *The European Physical Journal C* **78** (2018) 838 [[1803.11210](#)].

[37] K. J. Bae, H. Baer and H. Serce, *Prospects for axion detection in natural SUSY with mixed axion-higgsino dark matter: Back to invisible?*, *Journal of Cosmology and Astroparticle Physics* **06** (2017) 024 [[1705.01134](#)].

[38] H. Baer, *Radiative natural supersymmetry with mixed axion/higgsino cold dark matter*, in *AIP Conf. Proc.*, vol. 1534, pp. 39–46, May, 2013, [1210.7852](#), DOI.

[39] C. Han, *Higgsino Dark Matter in a Non-Standard History of the Universe*, *Phys. Lett. B* **798** (2019) 134997 [[1907.09235](#)].

[40] M. Cirelli, N. Fornengo and A. Strumia, *Minimal dark matter*, *Nucl. Phys. B* **753** (2006) 178 [[hep-ph/0512090](#)].

[41] P. J. Fox, G. D. Kribs and A. Martin, *Split Dirac Supersymmetry: An Ultraviolet Completion of Higgsino Dark Matter*, *Phys. Rev. D* **90** (2014) 075006 [[1405.3692](#)].

[42] N. Arkani-Hamed and S. Dimopoulos, *Supersymmetric unification without low energy supersymmetry and signatures for fine-tuning at the LHC*, *JHEP* **06** (2005) 073 [[hep-th/0405159](#)].

[43] G. F. Giudice and A. Romanino, *Split supersymmetry*, *Nucl. Phys. B* **699** (2004) 65 [[hep-ph/0406088](#)].

[44] N. Arkani-Hamed, S. Dimopoulos, G. F. Giudice and A. Romanino, *Aspects of split supersymmetry*, *Nucl. Phys. B* **709** (2005) 3 [[hep-ph/0409232](#)].

[45] N. Arkani-Hamed, A. Delgado and G. F. Giudice, *The Well-Tempered Neutralino*, *Nucl. Phys. B* **741** (2006) 108 [[hep-ph/0601041](#)].

[46] M. Chakraborti, U. Chattopadhyay, S. Rao and D. P. Roy, *Higgsino Dark Matter in Nonuniversal Gaugino Mass Models*, *Physical Review D* **91** (2015) 035022 [[1411.4517](#)].

[47] Q. Shafi, A. Tiwari and C. S. Un, *Third family quasi-Yukawa unification: Higgsino dark matter, NLSP gluino and all that*, [2302.02905](#).

[48] V. S. Mummidi and K. M. Patel, *Pseudo-Dirac Higgsino dark matter in GUT scale supersymmetry*, *Journal of High Energy Physics* **01** (2019) 224 [[1811.06297](#)].

[49] K. Griest and D. Seckel, *Three exceptions in the calculation of relic abundances*, *Phys. Rev. D* **43** (1991) 3191.

[50] M. J. Baker et al., *The coannihilation codex*, *JHEP* **12** (2015) 120 [[1510.03434](#)].

[51] M. Chakraborti, U. Chattopadhyay and S. Poddar, *How light a higgsino or a wino dark matter can become in a compressed scenario of MSSM*, *Journal of High Energy Physics* **09** (2017) 064 [[1702.03954](#)].

[52] LZ collaboration, J. Aalbers et al., *First Dark Matter Search Results from the LUX-ZEPLIN (LZ) Experiment*, *Phys. Rev. Lett.* **131** (2023) 041002 [[2207.03764](#)].

[53] LZ collaboration, J. Aalbers et al., *Dark Matter Search Results from 4.2 Tonne-Years of Exposure of the LUX-ZEPLIN (LZ) Experiment*, [2410.17036](#).

[54] C. Cheung, L. J. Hall, D. Pinner and J. T. Ruderman, *Prospects and Blind Spots for Neutralino Dark Matter*, *JHEP* **05** (2013) 100 [[1211.4873](#)].

[55] T. Han, F. Kling, S. Su and Y. Wu, *Unblinding the dark matter blind spots*, *JHEP* **02** (2017) 057 [[1612.02387](#)].

[56] P. Huang and C. E. M. Wagner, *Blind Spots for neutralino Dark Matter in the MSSM with an intermediate m_A* , *Phys. Rev. D* **90** (2014) 015018 [[1404.0392](#)].

[57] B. Feldstein, P. W. Graham and S. Rajendran, *Luminous Dark Matter*, *Phys. Rev. D* **82** (2010) 075019 [[1008.1988](#)].

[58] D. Tucker-Smith and N. Weiner, *Inelastic dark matter*, *Phys. Rev. D* **64** (2001) 043502 [[hep-ph/0101138](#)].

[59] P. W. Graham, H. Ramani and S. S. Y. Wong, *Enhancing direct detection of Higgsino dark matter*, *Phys. Rev. D* **111** (2025) 055030 [[2409.07768](#)].

[60] G. Bertone, D. Hooper and J. Silk, *Particle dark matter: Evidence, candidates and constraints*, *Phys. Rept.* **405** (2005) 279 [[hep-ph/0404175](#)].

[61] S. Baum, M. Carena, N. R. Shah and C. E. Wagner, *Higgs portals for thermal Dark Matter. EFT perspectives and the NMSSM*, *JHEP* **04** (2018) 069 [[1712.09873](#)].

[62] J. Hisano, S. Matsumoto, M. M. Nojiri and O. Saito, *Direct detection of the Wino and Higgsino-like neutralino dark matters at one-loop level*, *Phys. Rev. D* **71** (2005) 015007 [[hep-ph/0407168](#)].

[63] L. Shang and Y. Zhang, *EasyScan-HEP: A tool for connecting programs to scan the parameter space of physics models*, *Comput. Phys. Commun.* **296** (2024) 109027 [[2304.03636](#)].

[64] F. Feroz, M. Hobson and M. Bridges, *Multinest: an efficient and robust bayesian inference tool for cosmology and particle physics*, *Monthly Notices of the Royal Astronomical Society* **398** (2009) 1601.

[65] F. Mahmoudi, J. Rathsman, O. Stal and L. Zeune, *Light Higgs bosons in phenomenological NMSSM*, *Eur. Phys. J. C* **71** (2011) 1608 [[1012.4490](#)].

[66] S. F. King, M. Muhlleitner and R. Nevezorov, *NMSSM Higgs Benchmarks Near 125 GeV*, *Nucl. Phys. B* **860** (2012) 207 [[1201.2671](#)].

[67] A. Arbey, M. Battaglia, F. Mahmoudi and D. Martínez Santos, *Supersymmetry confronts $B_s \rightarrow \mu^+ \mu^-$: Present and future status*, *Phys. Rev. D* **87** (2013) 035026 [[1212.4887](#)].

[68] ATLAS collaboration, G. Aad et al., *Combined measurements of Higgs boson production and decay using up to 80 fb^{-1} of proton-proton collision data at $\sqrt{s} = 13$ TeV collected with the ATLAS experiment*, *Phys. Rev. D* **101** (2020) 012002 [[1909.02845](#)].

[69] F. Mahmoudi, *Supersymmetry, direct and indirect constraints*, *Nucl. Part. Phys. Proc.* **303-305** (2018) 37 [[1812.08783](#)].

[70] PLANCK collaboration, N. Aghanim et al., *Planck 2018 results. VI. Cosmological parameters*, *Astron. Astrophys.* **641** (2020) A6 [[1807.06209](#)].

[71] P. Bechtle, O. Brein, S. Heinemeyer, G. Weiglein and K. E. Williams, *Higgsbounds: confronting arbitrary higgs sectors with exclusion bounds from lep and the tevatron*, *Computer Physics Communications* **181** (2010) 138.

[72] P. Bechtle, O. Brein, S. Heinemeyer, G. Weiglein and K. E. Williams, *Higgsbounds 2.0. 0: confronting neutral and charged higgs sector predictions with exclusion bounds from lep and the tevatron*, *Computer Physics Communications* **182** (2011) 2605.

[73] P. Bechtle, O. Brein, S. Heinemeyer, O. Stål, T. Stefaniak, G. Weiglein et al., *Higgsbounds-4: improved tests of extended higgs sectors against exclusion bounds from lep, the tevatron and the lhc*, *The European Physical Journal C* **74** (2014) 2693.

[74] P. Bechtle, S. Heinemeyer, O. Stål, T. Stefaniak and G. Weiglein, *Applying exclusion likelihoods from lhc searches to extended higgs sectors*, *The European Physical Journal C* **75** (2015) 421.

[75] P. Bechtle, S. Heinemeyer, O. Stål, T. Stefaniak and G. Weiglein, *Higgssignals: Confronting arbitrary higgs sectors with measurements at the tevatron and the lhc*, *The European Physical Journal C* **74** (2014) 2711.

[76] P. Bechtle, S. Heinemeyer, O. Stål, T. Stefaniak and G. Weiglein, *HiggsSignals: Confronting arbitrary Higgs sectors with measurements at the Tevatron and the LHC*, *Eur. Phys. J. C* **74** (2014) 2711 [[1305.1933](#)].

[77] O. Stål and T. Stefaniak, *Constraining extended Higgs sectors with HiggsSignals*, *PoS EPS-HEP2013* (2013) 314 [[1310.4039](#)].

[78] P. Bechtle, O. Brein, S. Heinemeyer, O. Stål, T. Stefaniak, G. Weiglein et al., *Recent Developments in HiggsBounds and a Preview of HiggsSignals*, *PoS CHARGED2012* (2012) 024 [[1301.2345](#)].

[79] H. Bahl, T. Biekötter, S. Heinemeyer, C. Li, S. Paasch, G. Weiglein et al., *HiggsTools: BSM scalar phenomenology with new versions of HiggsBounds and HiggsSignals*, *Comput. Phys. Commun.* **291** (2023) 108803 [[2210.09332](#)].

[80] W. Porod, F. Staub and A. Vicente, *A Flavor Kit for BSM models*, *Eur. Phys. J. C* **74** (2014) 2992 [[1405.1434](#)].

[81] PARTICLE DATA GROUP collaboration, P. Zyla et al., *Review of Particle Physics*, *PTEP* **2020** (2020) 083C01.

[82] W. Porod and F. Staub, *Spheno 3.1: extensions including flavour, cp-phases and models beyond the mssm*, *Computer Physics Communications* **183** (2012) 2458–2469.

[83] W. Porod, *SPheno, a program for calculating supersymmetric spectra, SUSY particle decays and SUSY particle production at e+ e- colliders*, *Comput. Phys. Commun.* **153** (2003) 275 [[hep-ph/0301101](#)].

[84] W. Porod and F. Staub, *SPheno 3.1: Extensions including flavour, CP-phases and models beyond the MSSM*, *Comput. Phys. Commun.* **183** (2012) 2458 [[1104.1573](#)].

[85] D. Barducci, G. Belanger, J. Bernon, F. Boudjema, J. Da Silva, S. Kraml et al., *Collider limits on new physics within micrOMEGAs-4.3*, *Comput. Phys. Commun.* **222** (2018) 327 [[1606.03834](#)].

[86] G. Bélanger, F. Boudjema, A. Pukhov and A. Semenov, *Dark matter direct detection rate in a generic model with micromegas2.2*, *Computer Physics Communications* **180** (2009) 747–767.

[87] G. Belanger, F. Boudjema, A. Pukhov and A. Semenov, *MicrOMEGAs: A Program for calculating the relic density in the MSSM*, *Comput. Phys. Commun.* **149** (2002) 103 [[hep-ph/0112278](#)].

[88] G. Belanger, F. Boudjema, A. Pukhov and A. Semenov, *micrOMEGAs: A Tool for dark matter studies*, *Nuovo Cim. C* **033N2** (2010) 111 [[1005.4133](#)].

[89] G. Belanger, F. Boudjema and A. Pukhov, *micrOMEGAs : a code for the calculation of Dark Matter properties in generic models of particle interaction*, in *The Dark Secrets of the Terascale: Proceedings, TASI 2011, Boulder, Colorado, USA, Jun 6 - Jul 11, 2011*, pp. 739–790, 2013, [1402.0787](#), DOI.

[90] G. Bélanger, F. Boudjema, A. Goudelis, A. Pukhov and B. Zaldivar, *micrOMEGAs5.0 : Freeze-in*, *Comput. Phys. Commun.* **231** (2018) 173 [[1801.03509](#)].

[91] F. Staub, *SARAH*, [0806.0538](#).

[92] F. Staub, *SARAH 3.2: Dirac Gauginos, UFO output, and more*, *Comput. Phys. Commun.* **184** (2013) 1792 [[1207.0906](#)].

[93] F. Staub, *SARAH 4 : A tool for (not only SUSY) model builders*, *Comput. Phys. Commun.* **185** (2014) 1773 [[1309.7223](#)].

[94] F. Staub, *Exploring new models in all detail with SARAH*, *Adv. High Energy Phys.* **2015** (2015) 840780 [[1503.04200](#)].

[95] C. A. J. O’Hare, *New Definition of the Neutrino Floor for Direct Dark Matter Searches*, *Phys. Rev. Lett.* **127** (2021) 251802 [[2109.03116](#)].

[96] J. Alwall, M. Herquet, F. Maltoni, O. Mattelaer and T. Stelzer, *Madgraph 5: going beyond*, *Journal of High Energy Physics* **2011** (2011) 128.

[97] J. Alwall, R. Frederix, S. Frixione, V. Hirschi, F. Maltoni, O. Mattelaer et al., *The automated computation of tree-level and next-to-leading order differential cross sections, and their matching to parton shower simulations*, *Journal of High Energy Physics* **2014** (2014) 79.

[98] C. Bierlich et al., *A comprehensive guide to the physics and usage of PYTHIA 8.3*, *SciPost Phys. Codeb.* **2022** (2022) 8 [[2203.11601](#)].

[99] T. Sjöstrand, S. Mrenna and P. Skands, *Pythia 6.4 physics and manual*, *Journal of High Energy Physics* **2006** (2006) 026.

[100] J. De Favereau, C. Delaere, P. Demin, A. Giannanco, V. Lemaitre, A. Mertens et al., *Delphes 3: a modular framework for fast simulation of a generic collider experiment*, *Journal of High Energy Physics* **2014** (2014) 57.

[101] D. Dercks, N. Desai, J. S. Kim, K. Rolbiecki, J. Tattersall and T. Weber, *CheckMATE 2: From the model to the limit*, *Comput. Phys. Commun.* **221** (2017) 383 [[1611.09856](#)].

[102] A. Aboubrahim, M. Klasen and P. Nath, *What the Fermilab muon $g-2$ experiment tells us about discovering supersymmetry at high luminosity and high energy upgrades to the LHC*, *Phys. Rev. D* **104** (2021) 035039 [[2104.03839](#)].

[103] M. Ackermann, A. Albert, B. Anderson, W. Atwood, L. Baldini, G. Barbiellini et al., *Searching for dark matter annihilation from milky way dwarf spheroidal galaxies with six years of fermi large area telescope data*, *Physical Review Letters* **115** (2015) 231301.

[104] FERMI-LAT collaboration, M. Ackermann et al., *Searching for Dark Matter Annihilation from Milky Way Dwarf Spheroidal Galaxies with Six Years of Fermi Large Area Telescope Data*, *Phys. Rev. Lett.* **115** (2015) 231301 [[1503.02641](#)].

[105] Y. Yue, J. Cao, F. Li and Z. Li, *Attractive features of Higgsino dark matter in the next-to-minimal supersymmetric standard model*, *Phys. Rev. D* **112** (2025) 095022 [[2503.10985](#)].